

Nanomechanical Investigations of Crystals of Copper Nanocluster Isomorphs: Enhanced Hardness of the Low-Density Analogue

Amoghavarsha Ramachandra Kini,[#] Sanghamitra Debta,[#] Arijit Jana,[#] C. Aparna, Vivek Yadav, Nataliia Kusiak, Tomas Base,^{*} Umesh V. Waghmare,^{*} Pijush Ghosh,^{*} and Thalappil Pradeep^{*}



Cite This: <https://doi.org/10.1021/acs.chemmater.4c03265>



Read Online

ACCESS |



Metrics & More

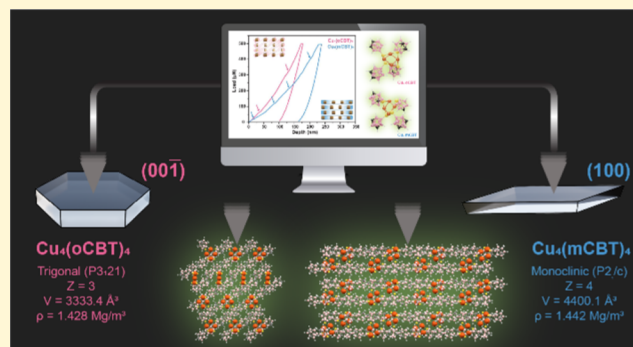


Article Recommendations



Supporting Information

ABSTRACT: Atomically precise cluster crystals, with constituent units composed of tens to hundreds of atoms, are important for the construction of miniaturized solid-state devices. Understanding the mechanical characteristics of such crystals is crucial for these applications. In this study, we focused on the nanomechanical properties of crystals of two isomorphous copper nanoclusters (Cu_4L_4), protected by *ortho*-carborane-9-thiol, $\text{Cu}_4(o\text{CBT})_4$, and *meta*-carborane-9-thiol, $\text{Cu}_4(m\text{CBT})_4$. These two clusters possess identical square planar Cu_4 cores embedded in butterfly-shaped Cu_4S_4 staples. Load–displacement measurements indicated that the crystals of $\text{Cu}_4(o\text{CBT})_4$ (hardness of ~ 534.31 MPa) were harder than those of $\text{Cu}_4(m\text{CBT})_4$ (hardness of ~ 335.49 MPa). Despite their lower density, crystals of $\text{Cu}_4(o\text{CBT})_4$ demonstrated increased hardness, owing to the presence of locked slanted layers that efficiently interacted with each other through various short contact supramolecular interactions. During indentation studies, multiple “pop-in” events were observed for the crystals of both clusters, suggesting the dislocation of molecular layers within the crystal lattice. Dynamic mechanical analysis conducted at different loading frequencies indicated that crystals of $\text{Cu}_4(o\text{CBT})_4$ have a higher storage modulus than $\text{Cu}_4(m\text{CBT})_4$. Both the crystals are thermally robust, as evident from thermogravimetric analysis and attenuated total reflection-IR analysis. Using density functional theory, we calculated Young’s modulus (E_r) for both crystals at 1 and 2% strain and found that the high-density isomorph had a lower E_r , consistent with experimental data showing E_r of $\text{Cu}_4(o\text{CBT})_4$ and $\text{Cu}_4(m\text{CBT})_4$ to be 9.79 and 8.54 GPa, respectively. These findings highlight the significant role of subtle structural differences in governing the nanomechanical behavior of isomorphous cluster crystals, paving the way for their rational design in advanced solid-state device applications.



INTRODUCTION

Atomically precise metal nanoclusters, particularly those composed of coinage metals, are a fascinating class of nanomaterials, well-known for their unique and finely tunable properties at the atomic scale.^{1–3} These nanoclusters exhibit quantum behavior, manifested by discrete electron energy levels and size-dependent optical properties, similar to molecules, due to their small size and precise atomic structure.⁴ Nanoclusters, typically made up of a few to several tens of atoms, display unique electrical,^{5–8} optical,^{9,10} magnetic,^{11–13} and catalytic^{14–16} properties that significantly distinguish them from both bulk materials and larger nanoparticles. These properties of nanoclusters make them ideal for various applications, ranging from highly efficient catalysts for chemical reactions to ultrasensitive sensors¹⁷ and novel electronic devices.¹⁸ Furthermore, atomically precise nanoclusters offer tunability in structure and properties that are hard to achieve with larger nanoparticles and/or bulk materials.

Nanoclusters can be synthesized by mixing metal salts and ligands in precise molar ratios, followed by the reduction of

metal ions using appropriate reducing agents in compatible solvents.^{19–21} By precisely controlling the number and nature of atoms within the nanoclusters, we can fine-tune their properties for specific applications. Ligands play an essential role in defining the properties of nanoclusters, and several types of ligands have been used to synthesize metal nanoclusters, such as phosphines,^{22,23} organic thiols,^{24,25} alkynes,^{26,27} proteins,^{28,29} and carboranethiols.^{30–32} Carboranethiol-protected metal clusters exhibit exceptional stability due to the thermally and chemically robust nature of carborane scaffolds. Structural stability is an essential characteristic for clusters to be used in nanodevices, and copper nanoclusters protected by carboranethiols represent one of the suitable

Received: November 28, 2024

Revised: January 10, 2025

Accepted: January 14, 2025

materials for electronics and other applications owing to their unique optical and catalytic properties and stability when exposed to elevated temperatures.³³

The physical, chemical, and mechanical properties of molecular crystals are intricately linked to their crystal structures, intermolecular interactions, and molecular orientations in the crystal.^{34–40} To study the mechanical properties of molecular materials, such as active pharmaceutical ingredients,^{35,41} metal–organic frameworks (MOFs),^{42–44} and perovskites,^{45,46} depth-sensing techniques are commonly employed. Molecular crystals tend to be very soft or prone to fracturing under stress, necessitating extremely small loads to study their mechanical properties. Therefore, nanoindentation is the most appropriate technique for investigating the mechanical behavior of such materials.³⁵ In nanoindentation, a sharp indenter tip is pressed into the surface of the material, leading to localized deformation, while the material's response to the applied load is recorded. Nanoclusters can act as building blocks for self-assembled solids, which can be precisely tuned at the atomic level by modifying the nanoclusters that constitute these structures. These self-assembled solids can be classified as molecular crystals, characterized by an ordered arrangement of nanoclusters with molecule-like properties.⁴⁷ Understanding the mechanical properties of nanocluster crystals is paramount for their use in nanoelectronic devices, although such studies are rare. Previous investigations have employed nanoindentation to explore the mechanical properties of Ag₂₉ and Ag_{40/46} nanocluster crystals.^{47,48} Nanoindentation experiments provide valuable insights into the hardness, elastic modulus, stiffness, and plastic deformation traits of the investigated material. These insights are instrumental in establishing structure–property relationships in nanoclusters.^{34–36}

Here, we present the nanoindentation studies of crystals of Cu₄ nanoclusters protected by *ortho*-carborane-9-thiol (*o*CBT) and *meta*-carborane-9-thiol (*m*CBT) to understand their mechanical properties under different static and dynamic loading conditions. The exceptional thermal stability and unique optical properties of Cu₄ nanoclusters prompted us to study their mechanical properties to find possible applications.³³ We performed various tests under load-controlled and displacement-controlled conditions and performed dynamical mechanical analyses, which are discussed in detail in subsequent sections. Our results suggest that Cu₄ nanoclusters protected by carboranethiol ligands have hardness and elastic modulus comparable to MOFs and organic crystals, making them more suitable for solid-state nanodevices and various other applications.

EXPERIMENTAL METHODS

Chemicals. The *o*CBT and *m*CBT were synthesized following the established procedures described in the literature.^{49,50} Copper iodide (CuI) and sodium borohydride (NaBH₄, 98%) were obtained from Aldrich Chemicals. 1,2-Bis(diphenylphosphino)ethane (DPPE) was purchased from Rankem Chemicals. Solvent-grade dichloromethane (DCM), acetone, acetonitrile, and methanol were procured from Rankem and Finar India. All chemicals used in this study were commercially available and used without further purification.

Synthesis of [Cu₁₈(DPPE)₆H₁₆]²⁺ Nanocluster. The [Cu₁₈(DPPE)₆H₁₆]²⁺ cluster, denoted as (Cu₁₈), was synthesized following the established procedure described in the literature.⁵¹ Initially, a mixture of 95 mg (0.49 mM) of CuI and 120 mg (0.03 mM) of DPPE was prepared under an argon atmosphere and dissolved in 15 mL of acetonitrile. After a reaction time of 30 min, the

resulting white complex was subjected to reduction by the direct addition of 180–185 mg of NaBH₄ powder. The reduction process was allowed to proceed for an additional 1 h with stirring at 750 rpm and room temperature. Subsequently, an orange-colored precipitate was observed, indicating the successful formation of the Cu₁₈ cluster. The reaction mixture was stirred for 6 h to isolate the desired product. Following this, the mixture was subjected to centrifugation, which resulted in the formation of an orange solid. The solid was washed three times using 5 mL of acetonitrile and methanol to remove any residual starting materials. Finally, the Cu₁₈ cluster, appearing as a dark orange-colored compound, was extracted using dichloromethane (DCM) for subsequent use in the LEIST reaction. The yield of the Cu₁₈ cluster was approximately 75% relative to that of the corresponding copper precursor.

Synthesis of Cu₄(*o*CBT)₄ and Cu₄(*m*CBT)₄ Clusters. Cu₄(*o*CBT)₄. The synthesis was done precisely as described in the literature.³³ Briefly, ~50 mg of the purified Cu₁₈ nanocluster was dissolved in 15 mL of dichloromethane (DCM) and reacted with 40 mg of *o*CBT at room temperature. After a reaction time of 2 h, the solution, initially yellowish in color, transformed, forming white precipitates. These white precipitates exhibited a vibrant green emission when subjected to a 365 nm UV lamp. The reaction was allowed to proceed for 5 h until completion. Subsequently, the microcrystalline white precipitates were thoroughly washed multiple times with methanol and DCM to eliminate any unreacted ligands present in excess. This white precipitate was soluble in acetone and was further purified by crystallization.

Cu₄(*m*CBT)₄. The synthesis of Cu₄(*m*CBT)₄ followed the same steps as above, but the ligand used was *m*CBT. The as-formed Cu₄(*m*CBT)₄ clusters were soluble in DCM. The reaction solvents were removed using rotavapor, and the solid white product that formed showed a green luminescence under a 365 nm UV lamp.

Crystallization of Cu₄(*o*CBT)₄ and Cu₄(*m*CBT)₄. Cu₄(*o*CBT)₄. The Cu₄(*o*CBT)₄ cluster is soluble only in acetone. Around 40 mg of the as-prepared cluster was dissolved in 2 mL of acetone. 2 mL of DCM (antisolvent) was added and mixed well with the cluster solution. A glass slide was kept to provide a substrate for crystallization. The solution was kept undisturbed in a 4 °C fridge. After 5–7 days, hexagonal crystals of Cu₄(*o*CBT)₄ were obtained, characterized by single-crystal X-ray diffraction (SC-XRD).

Cu₄(*m*CBT)₄. Around 40 mg of the as-prepared Cu₄(*m*CBT)₄ cluster was dissolved in 2 mL of DCM, and 1.5:1 (v/v) acetone and toluene (antisolvent) were mixed. A glass slide was kept to provide a substrate for crystallization. The solution was kept undisturbed in a 4 °C fridge. After 5–7 days, hundreds of parallelepiped crystals of Cu₄(*m*CBT)₄ were obtained, characterized by SC-XRD.

The crystals grown on the glass slides were directly used for nanoindentation experiments without any additional treatment.

Characterization. UV–Visible Spectroscopy. UV–vis absorption spectra of the clusters in their respective solution were recorded using a PerkinElmer Lambda 25 spectrophotometer in the 200–1100 nm wavelength range. The slit width used for the measurement is 1 nm. The cuvettes used had a thickness of 10 mm (path length). Measurements were conducted using solutions of Cu₄(*o*CBT)₄ in acetone and Cu₄(*m*CBT)₄ in dichloromethane.

SC-XRD (Face Indexing). SC-XRD data collection of Cu₄ clusters was performed with a Bruker D8 VENTURE single-crystal X-ray diffractometer equipped with a graphite monochromatic Mo (K α) (λ = 0.71073 Å) radiation and a PHOTON 100 CMOS detector. The data collection for both crystals was performed at 296 K. Face indexing was carried out by capturing a video of the crystals on the goniometer, and the faces were indexed using APEX software.

We did not conduct postindentation crystal structure analysis for crystals **1** and **2** because of the highly localized nature of the deformation caused by nanoindentation, which has minimal impact on the overall crystal structure. The indentation process can alter the structure in a small region at the indentation tip, known as the plastic zone, but probing this tiny volume would require specialized in situ

SC-XRD facilities. Instead, we investigated structural changes within the plastic region through computational studies.

Photoluminescence Spectroscopy. Photoluminescence spectra were measured using Horiba Jobin Nanolog spectrometer by applying a 3 nm bandpass filter having a resolution bandwidth of 5 nm. The Nanolog instrument has a 450 W xenon-arc lamp source, double monochromator with gratings, associated reflective optics, and a CCD detector. Solid samples were used for photoluminescence measurements as the samples show crystallization-induced luminescence.

X-ray Photoelectron Spectroscopy. X-ray photoelectron spectroscopy (XPS) was conducted using an Omicron Nanotechnology ESCA probe TPD spectrometer equipped with a polychromatic dual X-ray source of Mg $K\alpha$ ($h\nu = 1253.6$ eV) and Al $K\alpha$ ($h\nu = 1486.6$ eV). Al $K\alpha$ was used for the measurements of both crystals, which were drop-cast onto sample grids. The binding energies of all spectral regions were calibrated relative to the C 1s peak at 284.8 eV. The survey spectrum was acquired by using a pass energy of 50 eV with a step size of 0.5 eV. High-resolution scans for all elements were recorded at a pass energy of 20 eV and a step size of 0.08 eV to ensure precise peak resolution. Additionally, Cu LMM Auger spectra were collected for both samples to determine the oxidation state of copper in the nanocluster. These spectra were obtained by using a pass energy of 20 eV and a step size of 0.08 eV.

Attenuated Total Reflectance Infrared Spectroscopy. A PerkinElmer attenuated total reflectance infrared (ATR-IR) spectrometer was used to analyze the crystalline samples. Temperature-dependent chemical stability was assessed on heat-treated crystals that were heated to 150 °C. Measurements were taken just after heating the crystals at 30, 50, 80, 100, and 150 °C.

Thermogravimetric Analysis. Thermogravimetric measurements of about 5 mg of cluster sample in an alumina crucible were performed using NETZSCH STA 449 F3 Jupiter instruments equipped with Proteus-6.1.0 software. The measurements for both samples were performed under a nitrogen atmosphere at a flow rate of 20 mL/min in the temperature range of 30–700 °C with a heating rate of 10 °C/min.

Optical Microscopic Images. Optical microscopic images of the crystal were collected at different magnifications using a LEICA optical microscope equipped with LAS V4.8 software. A UV light (365 nm) was used to record luminescence images of the crystals.

Nanoindentation Measurements. The nanoindentation experiments were performed by using a Hysitron TI Premier nanomechanical testing instrument. We used a Berkovich indenter with a radius of 150 nm for nanomechanical measurements. Before the measurements, the nanoindenter was calibrated using a quartz crystal with a hardness value of 9.25 GPa. Indentation loads of 500, 1000, and 5000 μN were used with a trapezoidal load function. Among several different load functions used commonly in nanoindentation measurements, the trapezoidal load function is used commonly because of the linear loading segment, which ensures that the force is applied at a controlled rate. Also, molecular crystals can exhibit time-dependent behavior due to their softer and more ductile nature compared to metal and ceramic materials. The hold period in the trapezoidal load function allows time for any creep or time-dependent deformations to stabilize. This ensures that the unloading segment reflects only the elastic recovery, which leads to more accurate measurements of the hardness and elastic modulus. The unloading phase in the trapezoidal function is used to extract the elastic properties of the material by using gradual unloading of the nanoindenter from the sample. This gives an accurate load–displacement curve, which is important for analyzing the material's elastic modulus. All of these points also ensure that the data obtained are reproducible across multiple tests, making comparisons more reliable.^{52,53}

In situ scanning probe microscopy (SPM) was used to examine the surface topographies before and after indentation. The E_r and H were calculated by applying the Oliver and Pharr method, which used the initial part of the unloading segment of the load–displacement curve. Five crystals were indented in each sample. All measurements were

performed at 25 ± 2 °C in a temperature-controlled room maintained by air conditioning.

Nano Dynamic Mechanical Analysis Measurements. Dynamic mechanical analysis (DMA) was conducted in a load-controlled frequency sweep mode. An oscillating dynamic load of 10 μN was applied on top of a static load of 500 μN over a frequency range of 10–200 Hz. The storage modulus, loss modulus, and damping factors were determined by applying a sinusoidal force signal and recording the resulting displacement response.

Computational Details. First-principles density functional theory calculations were performed using the Vienna Ab initio Simulation Package (VASP)^{54–57} to study the mechanical properties of carboranethiol-protected nanoclusters $\text{Cu}_4(\text{oCBT})_4$ and $\text{Cu}_4(\text{mCBT})_4$. The interaction between the core and valence electrons was modeled using a projected augmented wave (PAW)^{58,59} potential, and exchange and correlation energy was treated using the Perdew–Burke–Ernzerhof (PBE) functional for a generalized gradient approximation (GGA).⁶⁰ Grimme's DFT-D3 scheme was employed to account for the effect of dispersion interactions.⁶¹ The energy cutoff for the plane wave basis was set to 520 eV, and a $1 \times 1 \times 1$ k -point grid centered at the Γ point was used in sampling Brillouin zone integration. A Fermi–Dirac function of width $k_B T = 0.05$ eV was employed to smear the discontinuity in occupation numbers of states near the Fermi level. The crystal structures of $\text{Cu}_4(\text{oCBT})_4$ and $\text{Cu}_4(\text{mCBT})_4$ are hexagonal and monoclinic, and they belong to the space groups $P3_121$ and $P2_1/c$, respectively. Structural optimization was carried out with the convergence threshold of energy and forces set to 10^{-8} eV and 10^{-3} eV/Å, respectively. Our estimates of lattice parameters and their experimental values are tabulated in Table S2. It is observed that they are less than the experimental values by 1–4%, which is in contrast to the expected trend from using GGA. This is attributed to the presence of solvents such as DCM, toluene, and acetone in the experimental samples. Since we plan to compare the properties of these two systems, these errors (being similar for both) will introduce systematic errors. However, the comparative trend should be reliable.

RESULTS AND DISCUSSION

Synthesis and Characterization of Cu_4 Nanoclusters.

Isomorphous Cu_4 nanoclusters protected by *ortho* and *meta*-carborane-9-thiol were synthesized according to our previously published study,³³ and herein, we discuss some essential structural features relevant to this investigation. Figure 1a shows a schematic of the synthesis of Cu_4 nanoclusters using the ligand-exchange-induced structural transformation (LEIST) method. A detailed LEIST synthesis procedure is provided in the Experimental Methods. $\text{Cu}_4(\text{oCBT})_4$ crystallizes as transparent hexagon-shaped crystals (referred to as 1), while $\text{Cu}_4(\text{mCBT})_4$ crystallizes as parallelepiped crystals (referred to as 2). Figure 1b,c shows optical microscopic images of the respective crystals under daylight and ultraviolet light.

The UV–vis optical absorption spectra of both nanoclusters exhibited a single absorption band around 275 nm (Figure S1). Emission spectra revealed characteristic emission bands peaking at 520 nm for $\text{Cu}_4(\text{oCBT})_4$ (1) and 532 nm for $\text{Cu}_4(\text{mCBT})_4$ (2) (Figure S2). Both nanoclusters displayed green photoluminescence under ultraviolet light, as shown in Figure 1b,c. The chemical purity of the samples was confirmed by using X-ray photoelectron spectroscopy (XPS) and ATR-IR spectroscopy. XPS survey spectra for 1 and 2 (Figures S3 and S4, respectively) confirmed the presence of the expected elements. High-resolution XPS scans were conducted for all of the key elements in both samples. In each case, the sulfur (S) peak corresponds to the metal-bound thiolate state. The Cu $2p_{3/2}$ peak appeared at 931.6 eV for nanocluster 1 and at 931.3

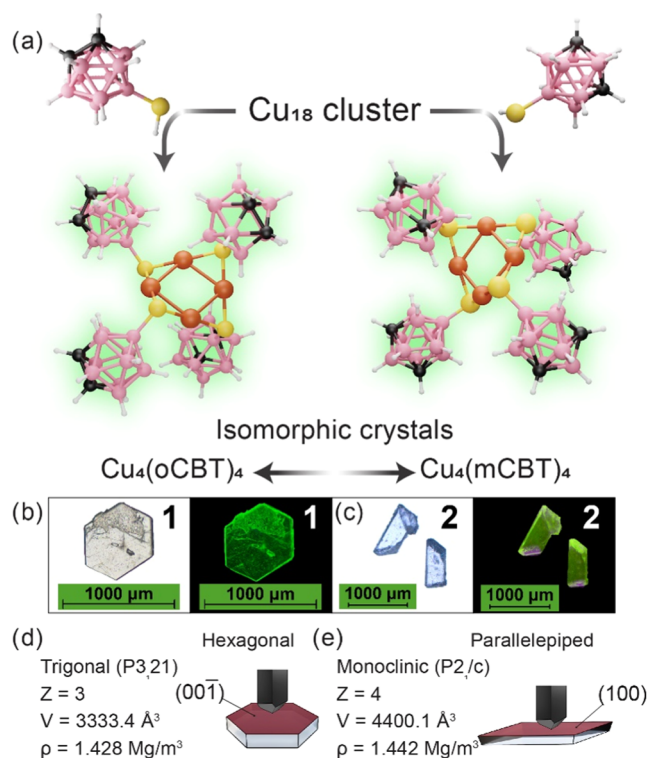


Figure 1. (a) Schematic representation of the synthesis of $\text{Cu}_4(\text{oCBT})_4$ and $\text{Cu}_4(\text{mCBT})_4$ from the Cu_{18} nanocluster through a LEIST reaction. Microscopic images of (b) $\text{Cu}_4(\text{oCBT})_4$ and (c) $\text{Cu}_4(\text{mCBT})_4$ single crystals under daylight and UV light. Labels 1 and 2 indicate the crystals of $\text{Cu}_4(\text{oCBT})_4$ and $\text{Cu}_4(\text{mCBT})_4$, respectively. The indented planes in these crystals are facing the reader. Scale bar: 1000 μm . Crystal parameters and the indented surfaces of the crystals of (d) $\text{Cu}_4(\text{oCBT})_4$ and (e) $\text{Cu}_4(\text{mCBT})_4$. Color codes: orange: copper, yellow: sulfur, pink: boron, black: carbon, and white: hydrogen.

eV for nanocluster 2. The absence of satellite peaks indicates that copper is in the +1 or 0 oxidation state. The oxidation state of Cu was further verified via a high-resolution scan of the Cu LMM Auger peak (Figures S3 and S4, insets), with peaks centered at approximately 915.5 and 915.4 eV for nanoclusters 1 and 2, respectively, consistent with the Cu^{+1} oxidation state.⁶²

The thermal stability of the nanoclusters was assessed using TGA, and these have been discussed previously.³³ Clusters 1 and 2 are stable up to 380 and 370 $^{\circ}\text{C}$, respectively. As an example, we present the data corresponding to cluster 2 in Supporting Figure S5. The mass loss of $\sim 65.59\%$ at 371.3 $^{\circ}\text{C}$ is assigned to the desorption of two carboranethiolate units and two carborane units, leaving behind Cu_2S as the residue. The

decomposition pathway of nanocluster 1 remains unclear, potentially due to the hypergolic activity of *o*-carborane moieties,³⁰ preventing the determination of the decomposition products. However, as the present study is independent of the nature of the decomposition products and high-temperature events, we did not pursue this aspect further. To further assess chemical stability at elevated temperatures, ATR-IR spectroscopy was performed on both samples. Spectra were recorded at 30, 50, 80, 100, and 150 $^{\circ}\text{C}$ to monitor any potential structural changes. No significant variations in the IR spectra were detected across this temperature range, confirming that both the nanoclusters retain their structural integrity under thermal treatment (Supporting Figures S6 and S7). These results underline the resilience of the nanoclusters under controlled heating conditions and provide insights into their potential applications in thermally demanding environments.

Structural Features of Cu_4 Nanoclusters. SC-XRD reveals that both clusters have nearly square planar cores of four Cu atoms with the average Cu–Cu distance of 2.6 \AA . The carboranethiols are attached to the square planar metal core through μ_2 sulfide linkages. The face indexing of the crystals was performed to identify the exposed planes of the crystals available for indentation. Finely shaped crystals were selected for face indexing. The indices of all of the crystal faces of 1 and 2 are shown in Figures S8 and S9, respectively. The indentation experiments were carried out on (001) and (100) surfaces of 1 and 2, respectively (marked in Figure 1d,e).

Figure 2a,b represents the extended packing configurations of nanoclusters 1 and 2 as viewed along the *a*- and *b*-axes, respectively. These figures also highlight the crystallographic planes where nanoindentation measurements were conducted. Figures 2a and S10 show that, in the extended packing structure of nanocluster 1, the clusters are arranged in slanted layers. The metallic cores are aligned linearly along a plane; however, the intercluster interactions predominantly occur along the slanted planes. Notably, each cluster is rotated by 120° along the *c*-axis (as observed from the *a*-axis perspective), compared to the cluster in the layer immediately above it, as shown in Figure S10a. Furthermore, the precise orientation of the cluster in the initial layer repeats in the fourth layer, demonstrating that nanocluster 1 exhibits an $\cdots\text{ABCABC}\cdots$ arrangement, as shown in Figures 2a and S10b.

In contrast, nanocluster 2 showcases a configuration where the clusters are organized in straight, parallel planes with intercluster interactions predominantly in the same plane, as shown in Figure 2b. Each cluster is rotated 180° along the *b*-axis (as viewed from the *b*-axis perspective) relative to the cluster in the layer above it, as illustrated in Figure S11a. When inspected from the *b*-axis, the exact orientation of the cluster in the first layer reappears in the third layer, following a complete

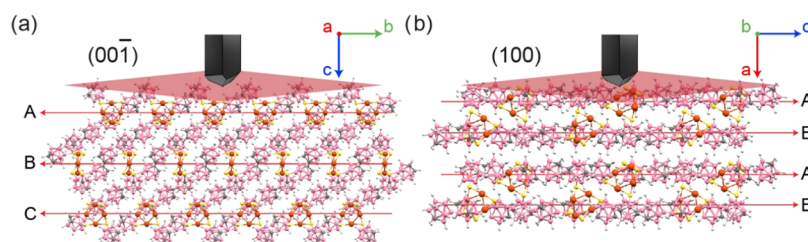


Figure 2. Extended supramolecular packing of (a) $\text{Cu}_4(\text{oCBT})_4$ (1) and (b) $\text{Cu}_4(\text{mCBT})_4$ (2) along the marked indentation planes. The $\cdots\text{ABCABC}\cdots$ and $\cdots\text{ABAB}\cdots$ packings of 1 and 2 are shown.

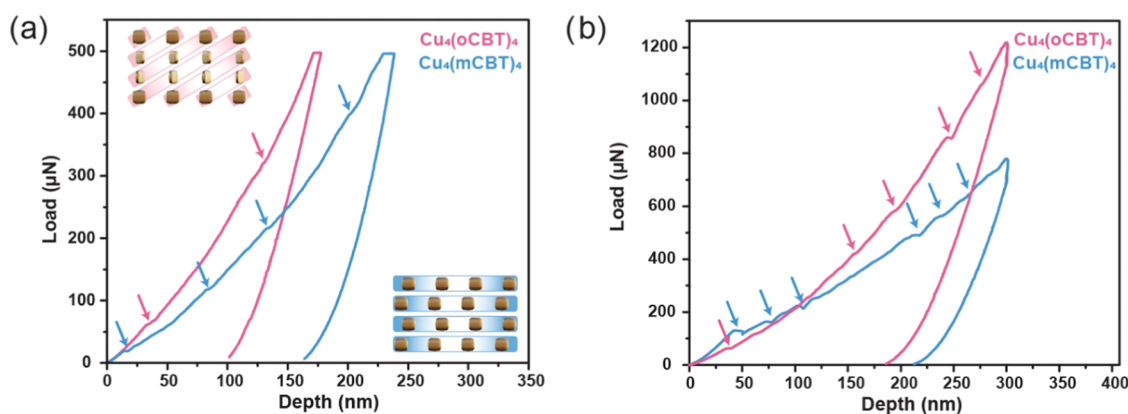


Figure 3. (a) Load–displacement curves of both crystals under a fixed load of 500 μN using a load function of 5–10–5 s. The inset shows the schematic packing diagram of $\text{Cu}_4(\text{oCBT})_4$ (top) and $\text{Cu}_4(\text{mCBT})_4$ (bottom). The differently oriented rectangles represent the clusters. (b) Load–displacement curves with a fixed displacement of 300 nm. Arrows indicate pop-in events occurring during nanoindentation experiments.

360° rotation. This pattern indicates that nanocluster 2 is arranged in an $\cdots\text{ABAB}\cdots$ fashion within its crystal lattice, as depicted in Figures 2b and S11b. Remarkably, the adjacent clusters exhibit a mirror-image symmetry when observed along the a -axis (Figure S11c,d).

Nanoindentation Studies on Crystals of Cu_4 Nanoclusters. The mechanical properties of the Cu_4 crystals were investigated by using a Hysitron TI 950 Triboindenter equipped with a 150 nm Berkovich tip. Before the measurements, the nanoindenter was calibrated using a quartz crystal with a hardness value of 9.25 GPa. Crystals 1 and 2 were directly grown onto a glass slide, and nanoindentation was performed on the single crystals as-prepared, i.e., without any additional treatment. While the literature suggests cleaving of the crystals before indentation measurements to reduce surface roughness, it was not feasible for this study due to the small size of the crystals. Moreover, the crystals were not subjected to solvent washing to avoid increasing surface roughness.³⁹ Indentation was performed on the (001) plane for cluster 1 and on the (100) plane for cluster 2. These specific planes were chosen since they are naturally exposed after crystal growth, while other planes remained inaccessible due to the dimensions of the crystals. Five crystals were indented for each sample with five indentations per crystal, to ensure a reproducible load–displacement response.

Quasi-static measurements were performed initially where the indenter is loaded onto the crystals smoothly without any frequency, while the dynamic measurements were done with frequency changes from 10 to 220 Hz. Load-controlled nanoindentation measurements were conducted by using loads of 500, 1000, and 5000 μN to assess the durability of the material under stress. Different loads were chosen to gain insight into the elastic properties of the material as a function of the load. A trapezoidal load function was employed for all measurements, characterized by varying loading rates. This was achieved by adjusting the loading–holding–unloading times to 5–10–5, 20–10–20, and 50–20–50 s, respectively. Similarly, displacement-controlled experiments were performed at 100, 300, and 500 nm depths, with displacement functions of 20–10–20 s. Stress relaxation, creep behavior, and dynamic mechanical analysis were performed to understand the time-dependent mechanical behavior of the crystals, which is discussed in more detail in the next section.

Mechanical Properties of Cu_4 Nanoclusters. At first, load-controlled nanoindentation studies were performed on both crystals at a fixed load of 500 μN with a trapezoidal load function of 5–10–5 s. The load–displacement curve (shown in Figure 3a) illustrates that the crystals of 1 and 2 exhibit displacements of approximately 175 and 225 nm, respectively, for the applied load of 500 μN . The difference in displacements suggests that the crystals of 2 are less stiff than those of 1. Crystals 1 and 2 also show residual displacements (strain present in the system after the removal of stress) of 100 and 170 nm, respectively. The load-controlled indentation measurements, with a load of 500 μN , were also performed at different load functions of 20–10–20 and 50–20–50, presented in Figure S12a,b, respectively. The load-controlled indentations were also carried out at higher loads of 1000 and 5000 μN at three different load functions of 5–10–5, 20–10–20, and 50–20–50, as shown in Figure S13. These measurements consistently indicate that crystal 2 is undergoing a larger displacement than crystal 1 for a given maximum load.

Similarly, displacement-controlled nanoindentation studies were performed at fixed displacements of 100, 300, and 500 nm. Figure 3b indicates the load–displacement curve obtained for a 300 nm constant displacement, and it indicates that the crystals of 1 need a higher load of 1200 μN , while crystals of 2 require only 700 μN to attain the same displacement. Figure S14 presents the load–displacement curves for 100 and 500 nm constant displacements, showing similar results. The difference in response between these two types of crystals can be attributed to the different arrangements of molecular planes in the crystals, shown in Figure 2a,b. In the case of 2, the planes are arranged perpendicular to the indentation direction, making them more susceptible to plastic deformation. Conversely, the planes of 1 are slanted relative to the indentation direction, and the clusters may be packed more effectively at the local deformation scale, rendering them more resistant to deformation.³⁵ Similarly, the molecular arrangement-dependent mechanical response was also observed in crystals of omeprazole,⁶³ Ag_{29} nanocluster,⁴⁷ and in the cocrystals of glutaric acid and caffeine.⁶⁴

We observed significant kinks in the measured load–displacement curves of both crystals, represented by arrows in Figure 3a,b. These kinks are called “pop-ins” and are characteristic of molecular crystals. They occur due to the slipping or breaking of crystal planes. Among the two crystals,

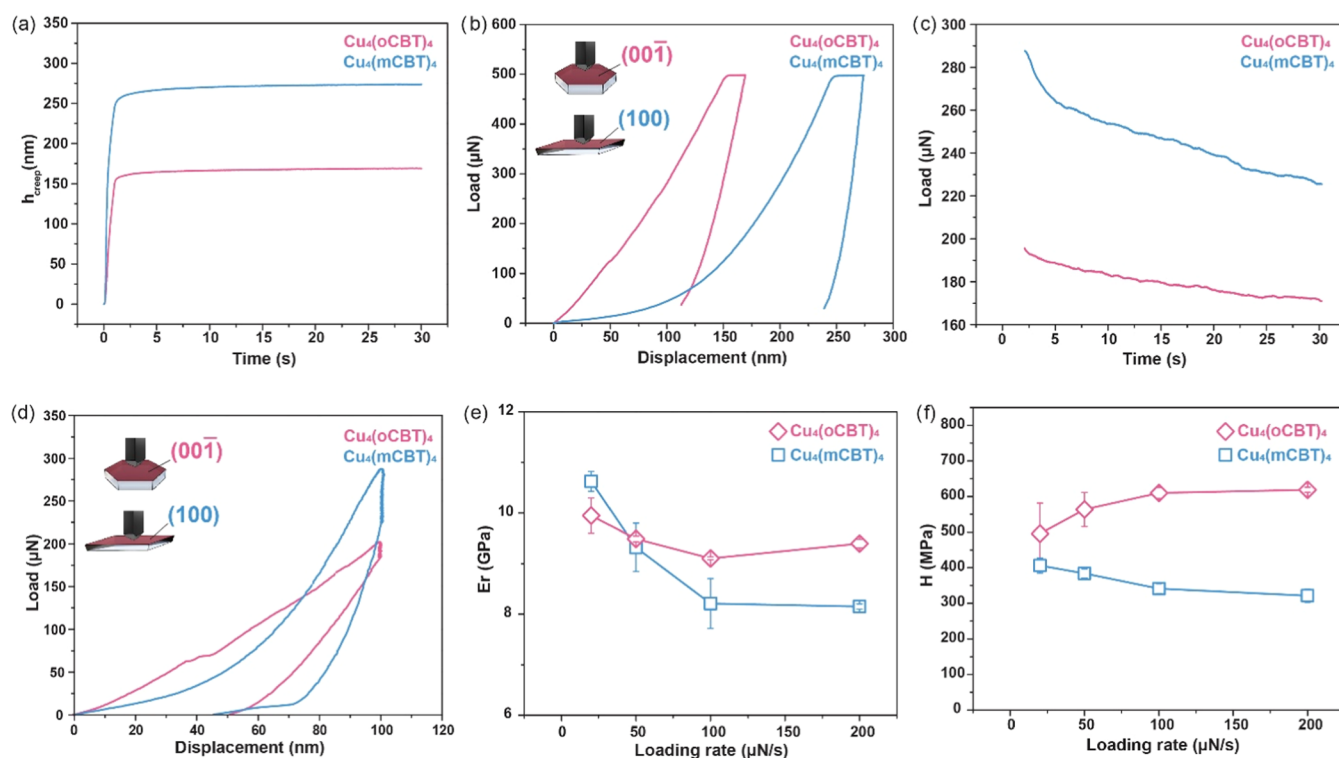


Figure 4. (a) Creep behavior as a function of time and (b) their corresponding load–displacement curves of $\text{Cu}_4(\text{oCBT})_4$ and $\text{Cu}_4(\text{mCBT})_4$ crystals with an applied load of $500 \mu\text{N}$. (c) Stress relaxation curves and (d) their corresponding load–displacement curves for $\text{Cu}_4(\text{oCBT})_4$ and $\text{Cu}_4(\text{mCBT})_4$ crystals with a fixed displacement of 100 nm . Variation of (e) Young's modulus (E_r) and (f) hardness (H) at different loading rates for $\text{Cu}_4(\text{oCBT})_4$ and $\text{Cu}_4(\text{mCBT})_4$ crystals. Insets in panels (b, c) show the plane of indentation in both the crystals.

2 shows more of these pop-ins than 1. The molecular planes of 2 tend to easily break or slip as they are perpendicular to the indentation direction, leading to “pop-in” events, while the slanted molecular planes of 1 are resistant to pop-ins as they can slide reasonably smoothly in the direction of indentation. Anisotropic molecular crystals exhibit similar direction-dependent mechanical behavior due to the arrangement of lattice planes.^{40,64} However, we could not access other crystal planes for our studies due to the difficulty of manipulating tiny crystals.

While most organic crystals can be characterized by their structural and optical properties, certain molecular crystals exhibit additional rheological characteristics such as creep, stress relaxation, and viscoelasticity, depending on the specific molecular structure and the applied load. Understanding these rheological properties is essential for their application in polymer science, materials engineering, and pharmaceuticals.^{47,48} Therefore, a comprehensive set of load and displacement-controlled tests were conducted to probe the rheological behavior of both the crystals. In order to study the creep behavior, the load was increased from 0 to $500 \mu\text{N}$ in 1 s and then held for another 30 s, and the displacement was measured. Figure 4a indicates the displacement vs time curve (creep behavior) of crystals 1 and 2. When a force of $500 \mu\text{N}$ was applied to crystals 1 and 2 in 1 s, they showed the characteristic displacement of 150 and 250 nm, respectively. In typical creep measurements, the initial prominent displacement peak represents the occurrence of primary creep, followed by secondary and tertiary creeps. The primary creep starts rapidly and slows with time, while secondary creep shows a uniform increase in displacement while holding the load. Tertiary creep has an increased creep rate and sets in when the material

breaks or ruptures. The secondary and tertiary creeps are usually found in materials like polymers, ceramics, concrete, and construction materials, especially at elevated temperatures.^{65,66} Both crystals show primary creep with large initial displacement, as indicated in Figure 4a. However, there are no signs of secondary or tertiary creeps as the displacement remains constant for the entire time the indenter tip is held in position. This indicates that the crystals resist continuous deformation and are stable under stress.

Similarly, stress relaxation tests were also performed to investigate the relaxation behavior of the crystals. In these tests, a displacement of 100 nm was applied in 1 second and held for another 30 s. The resulting change in the stress over time was measured. Figure 4c represents the stress relaxation curve, where both crystals showed a decrease in load with time, indicating that the clusters rearrange in the crystal structure to gradually reduce their internal stress over time under a constant applied load. These provide insights into the time-dependent mechanical behavior of crystals 1 and 2. The load–displacement plots obtained from creep and stress relaxation tests (Figure 4b,d) demonstrated a higher residual displacement in the case of crystal 2, which provided evidence for the reduced hardness of 2 compared to that of 1. The insets in Figure 4b,d indicate the planes on which the indentations were carried out.

Multiple indentation tests were performed on the crystals of both nanoclusters to accurately assess their nanomechanical behavior. The load–displacement curves collected at various indentation loads, as shown in Figure S15, demonstrate reproducibility across the tests. These curves were subsequently used to determine the reduced modulus (E_r) and hardness (H) of the crystals. Figures S16 and S17 present a

Table 1. Measured Hardness and Young's Modulus in Single Crystals of Isomorphous Cu₄ Nanoclusters along with Other Nanoclusters Studied to Date¹

| cluster | crystal system | ρ (g cm ⁻³) | H (MPa) | E_r (GPa) | ref |
|---|----------------|------------------------------|----------------|-------------|-----------|
| [Ag ₄₆ (2,5-DMBT) ₂₄ (PPh ₃) ₈] ²⁺ | trigonal | 1.322 | 168.10 ± 25.52 | 2.27 ± 0.25 | 47 |
| cocrystals of [Ag ₄₆ (2,5-DMBT) ₂₄ (PPh ₃) ₈] ²⁺ and [Ag ₄₀ (2,4-DMBT) ₂₄ (PPh ₃) ₈] ³⁺ | monoclinic | 1.497 | 166.70 ± 28.02 | 2.73 ± 0.51 | 47 |
| [Ag ₂₉ (1,3-BDT) ₁₂ (PPh ₃) ₄] ³⁻ | cubic | 2.11 | 282.19 ± 53.33 | 5.66 ± 0.44 | 48 |
| [Ag ₂₉ (1,3-BDT) ₁₂ (PPh ₃) ₄] ³⁻ | trigonal | 2.04 | 498.15 ± 23.61 | 7.53 ± 0.41 | 48 |
| Cu ₄ (oCBT) ₄ | trigonal | 1.428 | 534.31 ± 82.48 | 9.79 ± 0.98 | this work |
| Cu ₄ (mCBT) ₄ | monoclinic | 1.442 | 335.49 ± 68.68 | 8.54 ± 0.73 | this work |

¹(Abbreviations: 2,5-DMBT—2,5-dimethylbenzenethiol, 2,4-DMBT—2,4-dimethylbenzenethiol, 1,3-BDT—1,3-benzenedithiol, and PPh₃—triphenylphosphine).

statistical analysis of the data for clusters **1** and **2**, respectively. The mean E_r values were 9.79 ± 0.98 GPa for cluster **1** and 8.54 ± 0.73 GPa for cluster **2**, while the corresponding hardness values were 534.31 ± 82.48 and 335.49 ± 68.68 MPa, respectively. The histograms illustrate the distribution of E_r and H values for the crystals, with overlaid Gaussian fits that suggest a normal distribution pattern. This Gaussian distribution supports the reliability and consistency of the measurements, validating the reproducibility of the nanomechanical properties observed across the data set. We have compiled the E_r and H values of various nanoclusters studied to date, in Table 1, to illustrate the range of these mechanical properties across different nanoclusters.

Both crystals, like viscoelastic materials, manifest stress relaxation behavior over a holding time (Figure 4c). However, this behavior was not very pronounced in the creep vs time plot (Figure 4a), indicating that the material gradually released its internal stresses when exposed to a constant applied load while avoiding significant and continuous deformation. Materials such as elastomers and thermosetting polymers display this behavior characterized by stress relaxation without significant creep. Elastomers quickly adapt to deformed states and revert to their original form upon removal of the deforming force, thus exhibiting stress relaxation. Similarly, thermosetting polymers resist flow and permanent deformation under sustained loads due to their rigid cross-linked network, allowing them to demonstrate stress relaxation while preventing significant creep.^{67–69}

Stress reduction in molecular crystals can have various mechanisms, such as readjustment or rearrangement within the crystal lattices through molecular rotations and acoustic vibrations, leading to decreased overall stress.^{47,70,71} As for viscoelastic materials, the stress is proportional to the strain rate. Hence, indentation tests were performed at different loading rates to quantify the relationship between stress and the loading rate on the crystals (Figures S12–S14). The values of E_r and H at various loading rates are depicted in Figure 4e,f. It is noted from Figure 4e that for both **1** and **2**, the value of Young's modulus (E_r) decreases with an increase in the loading rate until 100 $\mu\text{N/s}$ and remains constant after that. An interesting behavior was observed for the crystals of **2** at lower loading rates, where the E_r value was initially higher than that of **1**. This behavior can be explained by analyzing the stress relaxation plot. At lower loading rates, the crystals undergo gradual deformation, allowing the clusters within the crystal to reorganize and adjust their orientations to relieve the stress faster, as evident in the stress relaxation plot (Figure 4c). This results in a higher apparent E_r . However, as the loading rate increases, the available time for molecular or structural reorganization within the lattice decreases. Consequently, the

crystal's ability to fully adapt to the applied stress is limited, leading to a reduced apparent E_r .

Figure 4f represents the variation of hardness with loading rate and measures plastic deformation occurring in the crystal. The crystals of **2** show a gradual decrease in hardness with an increase in loading rate. However, crystals of **1** show an increase in hardness with respect to the loading rate, which can be explained by the favorable arrangement/orientation of crystal planes to resist plastic deformation. As presented in Figure 2a,b, the crystal planes are arranged slanting in **1** while perpendicular to the indentation direction in the case of **2**. In the crystals of **2**, with an increase in loading rate, the hardness decreases as the clusters have less time to relax and resist the incoming stress at a higher loading rate. However, in the case of **1**, the planes must slide along the adjacent planes, possibly leading to friction due to intercluster interactions, which increases as the loading rate increases. Hence, the indenter experiences more resistance from the crystal as the loading rate increases.

To understand the strain-hardening effect of the crystals, we indented the same region four times. Figure S18 shows the indentation-induced hardness in the crystals of both compounds **1** and **2**. Initial indentations on crystals can induce stresses in the material, and these stresses may undergo relaxation and redistribution with each subsequent indentation, leading to variations in the measured indentation depth.⁴⁷ Figure S18a shows the behavior of the crystals of **1**, and Figure S18b shows the behavior of the crystals of **2** under repeated indentations. The crystals of cluster **1** show an increase in hardness with repeated indentations, which is typically observed for molecular crystals that exhibit strain-hardening effects. In the case of **2**, the hardness increases with repeated indentation, but in the fourth indentation, we observed that the hardness dropped suddenly and was almost equal to that of the first indentation, as it traces the first curve closely, indicating that **2** (observed to be softer among the isomorphs) exhibits a gradual degradation effect. In contrast, **1** (harder among the isomorphs) shows a sudden change in hardness, suggesting that crystals of **1** become harder under stress, while there is a gradual increase in hardness of crystals of **2**, along with a sudden decrease in hardness, which may be due to sudden failure of molecular layers due to previous indentations.

Figures S19 and S20 illustrate the atomic force microscopy topography and surface features of samples **1** and **2**, respectively, after indentation. In crystal **1** (Figure S19), three triangular indentations are visible within a 10.000 μm scan with height variations from 0 to 157.9 nm. The lateral and vertical distances across indentation **2** are 1.47975 μm and 2.74226 nm, with roughness values of $R_a = 29.5845$ nm and $R_q = 33.7117$ nm. In crystal **2** (Figure S20), five indentations were

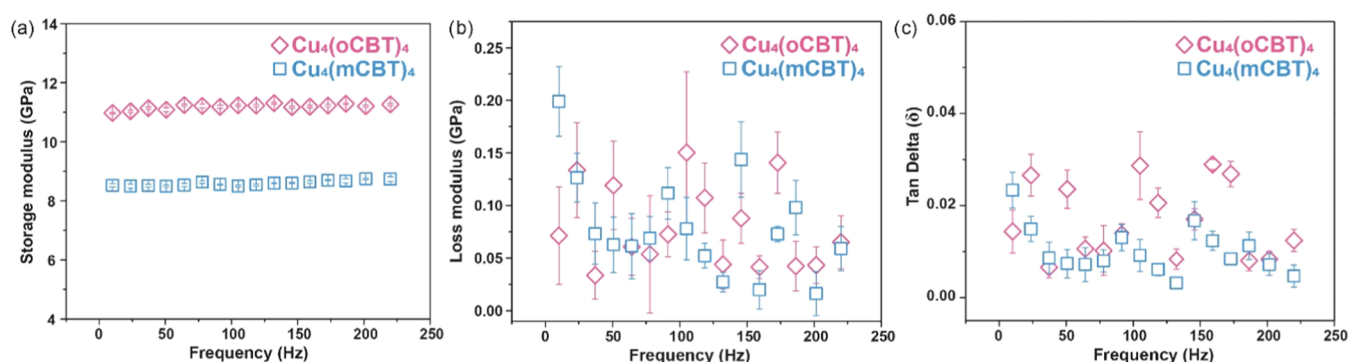


Figure 5. Frequency-dependent variations of (a) storage modulus, (b) loss modulus, and (c) tan delta (δ) observed through dynamic mechanical measurements of $\text{Cu}_4(\text{oCBT})_4$ and $\text{Cu}_4(\text{mCBT})_4$ crystals.

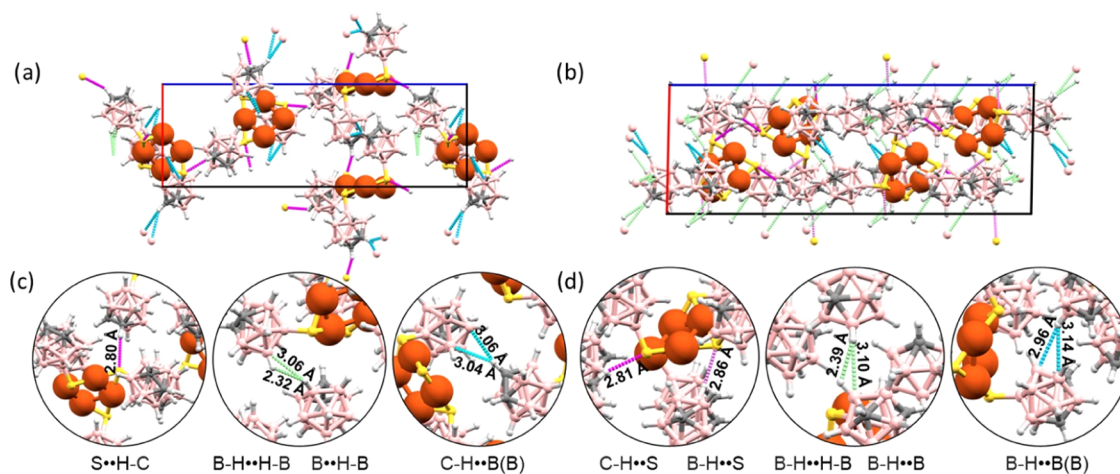


Figure 6. Unit cell supramolecular packing (as viewed along the *b*-axis) of (a) $\text{Cu}_4(\text{oCBT})_4$ and (b) $\text{Cu}_4(\text{mCBT})_4$ crystals along the *b*-axis. Different short contact intermolecular interactions of (c) $\text{Cu}_4(\text{oCBT})_4$ and (d) $\text{Cu}_4(\text{mCBT})_4$ clusters along with their interatomic distances. The colored dotted lines indicate intercluster interactions as follows: pink: $\text{S}\cdots\text{H}-\text{C}$ interaction, green: $\text{B}-\text{H}\cdots\text{H}-\text{B}$ and $\text{B}\cdots\text{H}$, B interactions, blue: $\text{C}-\text{H}\cdots\text{B}(\text{B})$ and $\text{B}-\text{H}\cdots\text{B}(\text{B})$ interactions.

performed within a 20.000 μm scan, with height variations from 0 to 1029.2 nm. The profile across indentation 1 has lateral and vertical distances of 3.51379 and 23.0089 nm and roughness values of $R_a = 90.8734$ nm and $R_q = 106.799$ nm, respectively. These findings suggest that crystal 2 has a rougher surface and potentially more variable indentation response, indicating differences in surface resilience and mechanical properties between the two crystal samples.

Dynamic Mechanical Analysis (DMA) of Isomorphous Cu_4 Nanoclusters. From the results of the quasi-static nanoindentation experiments, such as creep and stress relaxation behaviors discussed in the previous sections, it can be inferred that the crystals possess time-dependent properties. These results prompted us to conduct dynamic mechanical analysis tests at the same length scale. The different viscoelastic properties like storage modulus (G'), loss modulus (G''), and $\tan \delta$ are plotted as a function of frequency, as shown in Figure 5a–c, respectively. The storage modulus quantifies the energy stored within the system, while the loss modulus characterizes the energy dissipated or lost. $\tan \delta$ (Damping or loss factor) represents the phase shift between the applied stress and the resulting displacement and is the ratio between the loss and storage moduli. Figure 5a shows that the storage modulus for both crystals has no apparent frequency dependency, as the storage modulus values remain almost constant at all of the frequencies measured and are consistent with the higher mean

value of modulus obtained from quasi-static indentation. The loss modulus plot, Figure 5b, on the other hand, shows that the softer crystal 2 is more sensitive to frequency change than is 1.

Similarly, the low or almost negligible values of $\tan \delta$, as shown in Figure 5c, confirm that the crystals of both 1 and 2 exhibit very low energy dissipation and minimal phase lag between the applied stress and resulting strain. In other words, the crystals are highly elastic. These crystals can be used for applications like crystal optics, precision measurement instruments and machinery, mechanical resonators, and nano-mechanical instruments, where damping of vibrations is essential.^{72,73}

Structural Features Leading to Observed Mechanical Response. In our study, we find that crystals of 1 are harder than those of 2, even though 2 has a density (1.442 g/cm^3) higher than that of 1 (1.428 g/cm^3). So, the mechanical properties of the nanocluster crystals are governed by other factors like the arrangement of clusters in the crystal with respect to indentation direction, interactions between the nanoclusters in the crystal, the relaxation modes of the clusters under stress, the characteristics of the ligands protecting the metal nanoclusters, and so on.

We examined the intercluster interactions within cluster crystals to elucidate their mechanical properties. Unlike Sugi et al.'s findings, our crystals lacked $\pi\cdots\pi$ interactions.⁴⁷ Instead, the interactions in crystals 1 and 2 include $\text{S}\cdots\text{H}-\text{C}$, $\text{B}-\text{H}\cdots$

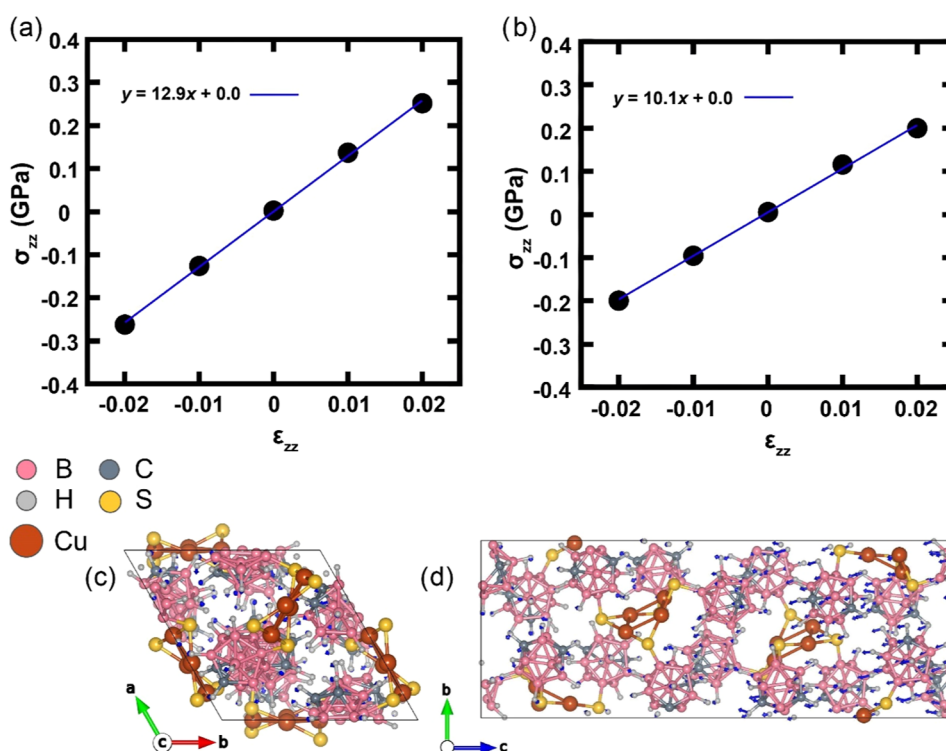


Figure 7. Stress vs strain curve is plotted for (a) $\text{Cu}_4(\text{oCBT})_4$ and (b) $\text{Cu}_4(\text{mCBT})_4$. Stress varies linearly with strain, and the slope of the curve gives the value of Young's modulus. Atomic rearrangement inside the lattice during structural optimization in (c) $\text{Cu}_4(\text{oCBT})_4$ and (d) $\text{Cu}_4(\text{mCBT})_4$. All displacements greater than 0.01 Å were incorporated and scaled up by a factor of 10 for better visualization.

H–B, C–H···B(B), and C–H···S, B–H···S, B–H···H–B, B–H···B, B–H···B(B), as shown in Figure 6a,b, respectively. These interactions contribute to the distinct mechanical responses of each crystal. The distances of each interaction are shown in the insets of Figure 6 as well as tabulated in Table S1 in the Supporting Information. These interactions are very weak interaction but still are responsible for the mechanical properties observed in both the crystals. In 1, the interactions are along the slant planes of the crystal, which slides along smoothly when indentation is carried out at lower loading rates while providing friction as the loading rate increases. However, the interactions in 2 are along the crystal planes and are perpendicular to the indentation direction. These planes cannot slide upon each other and hence have lesser stiffness than 1.

Further, DFT calculations were conducted to understand the response of the crystals to the applied stress. Specific details of the calculations are summarized in the Experimental Methods. Young's modulus (E_c) of 1 along $[hkl] = [00\bar{1}]$ and 2 along $[100]$ were estimated using the stress–strain method. Initially, a set of four distorted configurations corresponding to strains of ± 1 and $\pm 2\%$ along the c -axis (which lies along \hat{Z}) of 1 was generated. Clamping the structure along the strained direction, atomic positions, and the rest of the lattice parameters were allowed to relax. The stress σ_{zz} developed in the optimized structures was calculated, and its variation with strain ϵ_{zz} was used to estimate Young's modulus, E_{001} . This exercise was repeated for 2, but with a strain applied along the a -axis (which lies along \hat{x}), and E_{100} was estimated from σ_{xx} and ϵ_{xx} (Figure 7a,b). The linear nature of the plots in Figure 7a,b, indicates elastic behavior of the material within the applied strain range. The slopes of the linear fits represent the material's elastic moduli, and our estimates of E_{001} and E_{100} are

summarized in Table S3. It is clear that the E_{100} of 2 is lower than the E_{001} of 1, despite 2 having a higher density, aligning with our experimental findings. However, the bare elastic moduli calculated from stresses in the unrelaxed strained structures exhibit the opposite trend, as expected from their relative densities (Table S3). This suggests that the atomic rearrangement in 2 occurs at a larger scale than in 1 during structural optimization.

We trace the movement of atoms during optimization of structures corresponding to 1% applied strain for both crystals (Figure 7c,d). In $\text{Cu}_4(\text{oCBT})_4$, the H atoms attached to the CBT cage exhibit weak displacements toward the voids (Figure 7c). The square planar Cu_4 nanoclusters inside the crystal are arranged nearly perpendicular to the ab plane and lie along the direction of applied strain (Figure S21a). Examination of an isolated unit of $\text{Cu}_4(\text{oCBT})_4$ reveals that during structural optimization, this arrangement causes two of the oCBTs attached to adjacent vertices of the Cu nanocluster to roll inward and two others to roll outward. This effectively leads to the motion shown in Figure S21b. It is found that the degree of internal rearrangement in $\text{Cu}_4(\text{mCBT})_4$ is higher than that in $\text{Cu}_4(\text{oCBT})_4$. Besides this, we observe the directional and collective translational motion of atoms in the bc plane of $\text{Cu}_4(\text{mCBT})_4$ in some regions at different scales (Figure 7d). A cross section taken along the a -axis in the system shows that this is possible due to the nearly linear arrangement of mCBT attached to the Cu nanoclusters along the a direction (Figure S22), with gaps between them along both c and b directions, which allow for easy movement under strain. Our results explain the unexpected trend in Young's modulus observed in experiments and uncover the structural mechanisms of the mechanical response of these crystals. They suggest that these crystals are highly flexible,⁷⁴ somewhat akin to MOFs.

Additional investigations of these systems are underway in our laboratory.

Our previous work on the mechanical characteristics of nanocluster crystals has been expanded upon in this article. Together, these investigations demonstrate the distinct mechanical properties of nanocluster crystals and emphasize their enormous potential for a wide range of applications. These discoveries could be used to investigate the effects of ligands, dopant atoms, and environmental variables, such as temperature, on the mechanical properties of other relevant nanocluster materials. We successfully conducted nano-indentation studies on a specific plane for both the crystals. Attempts to explore additional planes were unsuccessful.

CONCLUSIONS

In conclusion, this study has provided valuable insights into the mechanical behavior of isomorphous crystals composed of tetranuclear copper clusters protected by isomeric carboranethiol ligands as investigated through nanoindentation experiments. Despite their closely related molecular structures, Cu_4 nanoclusters protected by *ortho*-carboranethiol exhibit superior rigidity and hardness compared to their *meta*-carboranethiol isomeric analogue. Notably, multiple “pop-in” events, particularly observed for the $\text{Cu}_4(\text{mCBT})_4$ cluster, suggest the translocation of lattice planes within the crystals upon loading. Additionally, dynamic mechanical studies have shed light on the storage moduli of these crystals. DFT calculations provide insights into the atomic dynamics under external stresses, elucidating the relaxation pathways governing the enhanced hardness observed within the low-density isomorph. Our findings indicate the critical role played by the orientation of lattice planes relative to the direction of the applied load and the interactions among clusters in determining the observed mechanical properties. These insights emphasize the precision in atomic arrangement within this class of copper clusters, characterized by exceptional stability, well-defined structures, and unprecedented control over their properties. These materials have the potential to significantly contribute to the forefront of modern materials science and nanotechnology, thus presenting a promising avenue for a broad range of applications.

ASSOCIATED CONTENT

Supporting Information

The Supporting Information is available free of charge at <https://pubs.acs.org/doi/10.1021/acs.chemmater.4c03265>.

Intercluster interactions, comparison of lattice parameters, computational calculations of E_p , UV–vis spectroscopy, PL spectroscopy, XPS, TGA, ATR-IR, face indexing, arrangement of clusters in crystal, load–displacement plots, statistical analysis, and SPM images (PDF)

AUTHOR INFORMATION

Corresponding Authors

Tomas Base – Department of Syntheses, Institute of Inorganic Chemistry, The Czech Academy of Sciences 1001, Husinec-Rez 25068, Czech Republic; orcid.org/0000-0003-2533-8705; Email: tbase@iic.acs.cz

Umesh V. Waghmare – Theoretical Sciences Unit and School of Advanced Materials (SAMat), Jawaharlal Nehru Centre for Advanced Scientific Research, Bengaluru 560064

Karnataka, India; orcid.org/0000-0002-9378-155X;

Email: waghmare@jncasr.ac.in

Pijush Ghosh – Department of Applied Mechanics and Biomedical Engg., Indian Institute of Technology Madras, Chennai 600036, India; orcid.org/0000-0002-6077-6498; Email: pijush@iitm.ac.in

Thalappil Pradeep – Department of Chemistry, DST Unit of Nanoscience (DST UNS) and Thematic Unit of Excellence (TUE), Indian Institute of Technology Madras, Chennai 600036, India; orcid.org/0000-0003-3174-534X; Email: pradeep@iitm.ac.in

Authors

Amoghavarsha Ramachandra Kini – Department of Chemistry, DST Unit of Nanoscience (DST UNS) and Thematic Unit of Excellence (TUE), Indian Institute of Technology Madras, Chennai 600036, India; orcid.org/0009-0003-6863-7729

Sanghamitra Debta – Department of Applied Mechanics and Biomedical Engg., Indian Institute of Technology Madras, Chennai 600036, India; orcid.org/0009-0003-6675-6783

Arijit Jana – Department of Chemistry, DST Unit of Nanoscience (DST UNS) and Thematic Unit of Excellence (TUE), Indian Institute of Technology Madras, Chennai 600036, India

C. Aparna – Theoretical Sciences Unit, Jawaharlal Nehru Centre for Advanced Scientific Research, Bengaluru 560064 Karnataka, India

Vivek Yadav – Department of Chemistry, DST Unit of Nanoscience (DST UNS) and Thematic Unit of Excellence (TUE), Indian Institute of Technology Madras, Chennai 600036, India

Nataliia Kusiak – Department of Syntheses, Institute of Inorganic Chemistry, The Czech Academy of Sciences 1001, Husinec-Rez 25068, Czech Republic

Complete contact information is available at:

<https://pubs.acs.org/doi/10.1021/acs.chemmater.4c03265>

Author Contributions

#A.R.K., S.D., and A.J. have contributed equally to this work. A.J., P.G., and T.P. suggested the idea. A.R.K., A.J., and V.Y. synthesized and characterized the materials. S.D. performed nanomechanical studies, and S.D. and A.R.K. performed the data analysis. N.K. and T.B. are responsible for the ligands used in this work. C.A. and U.V.W. carried out the computational studies. A.R.K. wrote the first draft of the manuscript with inputs from A.J. and S.D., and all of the authors finalized the manuscript. T.P., U.V.W., and P.G. conceptualized the project and finalized the manuscript.

Notes

The authors declare no competing financial interest.

ACKNOWLEDGMENTS

The authors acknowledge the support of the Science and Engineering Research Board (SERB), Department of Science and Technology (DST), and Government of India. T.P. acknowledges funding from the Centre of Excellence on Molecular Materials and Functions under the Institution of Eminence scheme of IIT Madras. T.P. thanks the Science and Engineering Research Board (SERB), India, for funding through the SPR/2021/000439 research grant. The authors

thank the Sophisticated Analytical Instruments Facility, IIT Madras, and Sudhadevi Antharjanam for the SC-XRD measurements. A.R.K. thanks the Council of Scientific and Industrial Research (CSIR) for his research fellowship. A.J. thanks IITM for his research fellowship. U.V.W. and T.P. acknowledge funding through their JC Bose Fellowships. C.A. acknowledges support from IKST, Bengaluru. V.Y. thanks the Ministry of Education for his Prime Minister's Research Fellowship.

DEDICATION

This article is dedicated to the Chemical Research Society of India in celebration of its 25th anniversary.

REFERENCES

- (1) Jin, R.; Zeng, C.; Zhou, M.; Chen, Y. Atomically Precise Colloidal Metal Nanoclusters and Nanoparticles: Fundamentals and Opportunities. *Chem. Rev.* **2016**, *116* (18), 10346–10413.
- (2) Chakraborty, I.; Pradeep, T. Atomically Precise Clusters of Noble Metals: Emerging Link between Atoms and Nanoparticles. *Chem. Rev.* **2017**, *117* (12), 8208–8271.
- (3) Kang, X.; Li, Y.; Zhu, M.; Jin, R. Atomically Precise Alloy Nanoclusters: Syntheses, Structures, and Properties. *Chem. Soc. Rev.* **2020**, *49* (17), 6443–6514.
- (4) Jana, A.; Kini, A. R.; Pradeep, T. Atomically Precise Clusters: Chemical Evolution of Molecular Matter at the Nanoscale. *AsiaChem Mag.* **2023**, *3* (1), 56–65, DOI: 10.51167/acm00040.
- (5) Reato, M.; Dainese, T.; Antonello, S.; Maran, F. Electron Transfer in Films of Atomically Precise Gold Nanoclusters. *Chem. Mater.* **2021**, *33* (11), 4177–4187.
- (6) Feng, A.; Hou, S.; Yan, J.; Wu, Q.; Tang, Y.; Yang, Y.; Shi, J.; Xiao, Z.-Y.; Lambert, C. J.; Zheng, N.; Hong, W. Conductance Growth of Single-Cluster Junctions with Increasing Sizes. *J. Am. Chem. Soc.* **2022**, *144* (34), 15680–15688.
- (7) Higaki, T.; Russell, J. C.; Paley, D. W.; Roy, X.; Jin, R. Electron Transport through Supercrystals of Atomically Precise Gold Nanoclusters: A Thermal Bi-Stability Effect. *Chem. Sci.* **2023**, *14*, 13191–13197.
- (8) Ji, S.; Peng, D.; Sun, F.; You, Q.; Wang, R.; Yan, N.; Zhou, Y.; Wang, W.; Tang, Q.; Xia, N.; Zeng, Z.; Wu, Z. Coexistent, Competing Tunneling, and Hopping Charge Transport in Compressed Metal Nanocluster Crystals. *J. Am. Chem. Soc.* **2023**, *145* (44), 24012–24020.
- (9) Jin, R. Atomically Precise Metal Nanoclusters: Stable Sizes and Optical Properties. *Nanoscale* **2015**, *7* (5), 1549–1565.
- (10) Aikens, C. M. Electronic and Geometric Structure, Optical Properties, and Excited State Behavior in Atomically Precise Thiolate-Stabilized Noble Metal Nanoclusters. *Acc. Chem. Res.* **2018**, *51* (12), 3065–3073.
- (11) De Nardi, M.; Antonello, S.; Jiang, D.; Pan, F.; Rissanen, K.; Ruzzi, M.; Venzo, A.; Zoleo, A.; Maran, F. Gold Nanowired: A Linear (Au₂₅)_n Polymer from Au₂₅ Molecular Clusters. *ACS Nano* **2014**, *8* (8), 8505–8512.
- (12) Agrachev, M.; Antonello, S.; Dainese, T.; Ruzzi, M.; Zoleo, A.; Aprà, E.; Govind, N.; Fortunelli, A.; Sementa, L.; Maran, F. Magnetic Ordering in Gold Nanoclusters. *ACS Omega* **2017**, *2* (6), 2607–2617.
- (13) Tian, S.; Liao, L.; Yuan, J.; Yao, C.; Chen, J.; Yang, J.; Wu, Z. Structures and Magnetism of Mono-Palladium and Mono-Platinum Doped Au₂₅ (PET)₁₈ Nanoclusters. *Chem. Commun.* **2016**, *52* (64), 9873–9876.
- (14) Du, Y.; Sheng, H.; Astruc, D.; Zhu, M. Atomically Precise Noble Metal Nanoclusters as Efficient Catalysts: A Bridge between Structure and Properties. *Chem. Rev.* **2020**, *120* (2), 526–622.
- (15) Jin, R.; Li, G.; Sharma, S.; Li, Y.; Du, X. Toward Active-Site Tailoring in Heterogeneous Catalysis by Atomically Precise Metal Nanoclusters with Crystallographic Structures. *Chem. Rev.* **2021**, *121* (2), 567–648.
- (16) Du, X.; Jin, R. Atomically Precise Metal Nanoclusters for Catalysis. *ACS Nano* **2019**, *13* (7), 7383–7387.
- (17) Jana, A.; Spoorthi, B. K.; Nair, A. S.; Nagar, A.; Pathak, B.; Base, T.; Pradeep, T. A Luminescent Cu₄ Cluster Film Grown by Electro Spray Deposition: A Nitroaromatic Vapour Sensor. *Nanoscale* **2023**, *15* (18), 8141–8147.
- (18) Yuan, P.; Zhang, R.; Selenius, E.; Ruan, P.; Yao, Y.; Zhou, Y.; Malola, S.; Häkkinen, H.; Teo, B. K.; Cao, Y.; Zheng, N. Solvent-Mediated Assembly of Atom-Precise Gold–Silver Nanoclusters to Semiconducting One-Dimensional Materials. *Nat. Commun.* **2020**, *11* (1), No. 2229.
- (19) Khatun, E.; Pradeep, T. New Routes for Multicomponent Atomically Precise Metal Nanoclusters. *ACS Omega* **2021**, *6* (1), 1–16.
- (20) Kini, A. R.; Pradeep, T. Chapter 8 - Synthesis of Atomically Precise Clusters. In *Atomically Precise Metal Nanoclusters*; Pradeep, T., Ed.; Elsevier, 2023; pp 157–176.
- (21) Yao, Q.; Cao, Y.; Chen, T.; Xie, J. Total Synthesis of Thiolate-Protected Noble Metal Nanoclusters. In *Atomically Precise Nanochemistry*; John Wiley & Sons, Ltd, 2023; pp 57–85.
- (22) Bootharaju, M. S.; Dey, R.; Gevers, L. E.; Hedhili, M. N.; Basset, J.-M.; Bakr, O. M. A New Class of Atomically Precise, Hydride-Rich Silver Nanoclusters Co-Protected by Phosphines. *J. Am. Chem. Soc.* **2016**, *138* (42), 13770–13773.
- (23) Yuan, S.-F.; Li, J.-J.; Guan, Z.-J.; Lei, Z.; Wang, Q.-M. Ultrastable Hydrido Gold Nanoclusters with the Protection of Phosphines. *Chem. Commun.* **2020**, *56* (51), 7037–7040.
- (24) Jin, R.; Zhao, S.; Xing, Y.; Jin, R. All-Thiolate-Protected Silver and Silver-Rich Alloy Nanoclusters with Atomic Precision: Stable Sizes, Structural Characterization and Optical Properties. *CrystEngComm* **2016**, *18* (22), 3996–4005.
- (25) Joshi, C. P.; Bootharaju, M. S.; Alhilaly, M. J.; Bakr, O. M. [Ag₂₅(SR)₁₈]⁻: The “Golden” Silver Nanoparticle. *J. Am. Chem. Soc.* **2015**, *137* (36), 11578–11581.
- (26) Guan, Z.-J.; Hu, F.; Li, J.-J.; Liu, Z.-R.; Wang, Q.-M. Homoleptic Alkynyl-Protected Gold Nanoclusters with Unusual Compositions and Structures. *Nanoscale* **2020**, *12* (25), 13346–13350.
- (27) Ma, X.; Xiong, L.; Qin, L.; Tang, Y.; Ma, G.; Pei, Y.; Tang, Z. A Homoleptic Alkynyl-Protected [Ag₉Cu₆(^tBuC–C)₁₂]⁺ Superatom with Free Electrons: Synthesis, Structure Analysis, and Different Properties Compared with the Au₇Ag₈ Cluster in the M₁₅⁺ Series. *Chem. Sci.* **2021**, *12* (38), 12819–12826.
- (28) Meng, X.; Zare, I.; Yan, X.; Fan, K. Protein-Protected Metal Nanoclusters: An Emerging Ultra-Small Nanozyme. *Wiley Interdiscip. Rev.: Nanomed. Nanobiotechnol.* **2020**, *12* (3), No. e1602.
- (29) Chen, X.; Ren, X.; Gao, X. Peptide or Protein-Protected Metal Nanoclusters for Therapeutic Application. *Chin. J. Chem.* **2022**, *40* (2), 267–274.
- (30) Wang, Q.-Y.; Wang, J.; Wang, S.; Wang, Z.-Y.; Cao, M.; He, C.-L.; Yang, J.-Q.; Zang, S.-Q.; Mak, T. C. W. O-Carborane-Based and Atomically Precise Metal Clusters as Hypergolic Materials. *J. Am. Chem. Soc.* **2020**, *142* (28), 12010–12014.
- (31) Jana, A.; Unnikrishnan, P. M.; Poonia, A. K.; Roy, J.; Jash, M.; Paramasivam, G.; Machacek, J.; Adarsh, K. N. V. D.; Base, T.; Pradeep, T. Carboranethiol-Protected Propeller-Shaped Photoresponsive Silver Nanomolecule. *Inorg. Chem.* **2022**, *61* (23), 8593–8603.
- (32) Jana, A.; Jash, M.; Poonia, A. K.; Paramasivam, G.; Islam, M. R.; Chakraborty, P.; Antharjanam, S.; Machacek, J.; Ghosh, S.; Adarsh, K. N. V. D.; Base, T.; Pradeep, T. Light-Activated Intercluster Conversion of an Atomically Precise Silver Nanocluster. *ACS Nano* **2021**, *15*, 15781–15793.
- (33) Jana, A.; Jash, M.; Dar, W. A.; Roy, J.; Chakraborty, P.; Paramasivam, G.; Lebedkin, S.; Kirakci, K.; Manna, S.; Antharjanam, S.; Machacek, J.; Kucerakova, M.; Ghosh, S.; Lang, K.; Kappes, M. M.; Base, T.; Pradeep, T. Carborane-Thiol Protected Copper Nanoclusters: Stimuli-Responsive Materials with Tunable Phosphorescence. *Chem. Sci.* **2023**, *14* (6), 1613–1626.

- (34) Reddy, C. M.; Rama Krishna, G.; Ghosh, S. Mechanical Properties of Molecular Crystals—Applications to Crystal Engineering. *CrystEngComm* **2010**, *12* (8), 2296.
- (35) Varughese, S.; Kiran, M. S. R. N.; Ramamurty, U.; Desiraju, G. R. Nanoindentation in Crystal Engineering: Quantifying Mechanical Properties of Molecular Crystals. *Angew. Chem., Int. Ed.* **2013**, *52* (10), 2701–2712.
- (36) Ramamurty, U.; Jang, J. Nanoindentation for Probing the Mechanical Behavior of Molecular Crystals—a Review of the Technique and How to Use It. *CrystEngComm* **2014**, *16* (1), 12–23.
- (37) Saha, S.; Mishra, M. K.; Reddy, C. M.; Desiraju, G. R. From Molecules to Interactions to Crystal Engineering: Mechanical Properties of Organic Solids. *Acc. Chem. Res.* **2018**, *51* (11), 2957–2967.
- (38) Gabriele, B. P. A.; Williams, C. J.; Lauer, M. E.; Derby, B.; Cruz-Cabeza, A. J. Isomechanical Groups in Molecular Crystals and Role of Aromatic Interactions. *Cryst. Growth Des.* **2020**, *20* (11), 7516–7525.
- (39) Gabriele, B. P. A.; Williams, C. J.; Lauer, M. E.; Derby, B.; Cruz-Cabeza, A. J. Nanoindentation of Molecular Crystals: Lessons Learned from Aspirin. *Cryst. Growth Des.* **2020**, *20* (9), 5956–5966.
- (40) Gabriele, B. P. A.; Williams, C. J.; Lauer, M. E.; Derby, B.; Cruz-Cabeza, A. J. Impact of Polymorphism on Mechanical Properties of Molecular Crystals: A Study of *p*-Amino and *p*-Nitro Benzoic Acid with Nanoindentation. *CrystEngComm* **2021**, *23* (10), 2027–2033.
- (41) Mishra, M. K.; Varughese, S.; Ramamurty, U.; Desiraju, G. R. Odd–Even Effect in the Elastic Moduli of α,ω -Alkanedicarboxylic Acids. *J. Am. Chem. Soc.* **2013**, *135* (22), 8121–8124.
- (42) Spencer, E. C.; Kiran, M. S. R. N.; Li, W.; Ramamurty, U.; Ross, N. L.; Cheetham, A. K. Pressure-Induced Bond Rearrangement and Reversible Phase Transformation in a Metal–Organic Framework. *Angew. Chem., Int. Ed.* **2014**, *53* (22), 5583–5586.
- (43) Tan, J. C.; Bennett, T. D.; Cheetham, A. K. Chemical Structure, Network Topology, and Porosity Effects on the Mechanical Properties of Zeolitic Imidazolate Frameworks. *Proc. Natl. Acad. Sci. U.S.A.* **2010**, *107* (22), 9938–9943.
- (44) Kanoo, P.; Mishra, M. K.; Hazra, A. Probing Time Dependent Phase Transformation in a Flexible Metal–Organic Framework with Nanoindentation. *Dalton Trans.* **2021**, *50* (33), 11380–11384.
- (45) Ma, L.; Li, W.; Yang, K.; Bi, J.; Feng, J.; Zhang, J.; Yan, Z.; Zhou, X.; Liu, C.; Ji, Y.; Huang, J. C.; Han, X. A - or X-Site Mixture on Mechanical Properties of A Pb X₃ Perovskite Single Crystals. *APL Mater.* **2021**, *9* (4), No. 041112.
- (46) Rosenhek-Goldian, I.; Cahen, D.; Cohen, S. R. Measuring and Understanding the Nanomechanical Properties of Halide Perovskites and Their Correlation to Structure—A Perspective. *J. Vac. Sci. Technol. B* **2023**, *41* (5), No. 058501.
- (47) Sugi, K. S.; Bandyopadhyay, P.; Bodiuzzaman, M.; Nag, A.; Hridya, M.; Dar, W. A.; Ghosh, P.; Pradeep, T. Manifestation of Structural Differences of Atomically Precise Cluster-Assembled Solids in Their Mechanical Properties. *Chem. Mater.* **2020**, *32* (18), 7973–7984.
- (48) Sugi, K. S.; Mallikarjunachari, G.; Som, A.; Ghosh, P.; Pradeep, T. Probing the Mechanical Response of Luminescent Dithiol-Protected Ag₂₉(BDT)₁₂(TPP)₄ Cluster Crystals. *ChemNanoMat* **2018**, *4* (4), 401–408.
- (49) Plešek, J.; Janoušek, Z.; Heřmánek, S. Chemistry of 9-Mercapto-1,7-Dicarba-Closo-Dodecaborane. *Collect. Czech. Chem. Commun.* **1978**, *43* (5), 1332–1338.
- (50) Plešek, J.; Heřmánek, S. Syntheses and Properties of Substituted Icosahedral Carborane Thiols. *Collect. Czech. Chem. Commun.* **1981**, *46* (3), 687–692.
- (51) Li, J.; Ma, H. Z.; Reid, G. E.; Edwards, A. J.; Hong, Y.; White, J. M.; Mulder, R. J.; O’Hair, R. A. J. Synthesis and X-Ray Crystallographic Characterisation of Frustum-Shaped Ligated [Cu₁₈H₁₆(DPPE)₆]²⁺ and [Cu₁₆H₁₄(DPPA)₆]²⁺ Nanoclusters and Studies on Their H₂ Evolution Reactions. *Chem. – Eur. J.* **2018**, *24* (9), 2070–2074.
- (52) Briscoe, B. J.; Fiori, L.; Pelillo, E. Nano-Indentation of Polymeric Surfaces. *J. Phys. D: Appl. Phys.* **1998**, *31* (19), 2395.
- (53) Klapperich, C.; Komvopoulos, K.; Pruitt, L. Nanomechanical Properties of Polymers Determined From Nanoindentation Experiments. *J. Tribol.* **2001**, *123* (3), 624–631.
- (54) Kresse, G.; Hafner, J. *Ab Initio* Molecular Dynamics for Liquid Metals. *Phys. Rev. B* **1993**, *47* (1), 558–561.
- (55) Kresse, G.; Hafner, J. *Ab Initio* Molecular-Dynamics Simulation of the Liquid-Metal–Amorphous-Semiconductor Transition in Germanium. *Phys. Rev. B* **1994**, *49* (20), 14251–14269.
- (56) Kresse, G.; Furthmüller, J. Efficient Iterative Schemes for *Ab Initio* Total-Energy Calculations Using a Plane-Wave Basis Set. *Phys. Rev. B* **1996**, *54* (16), 11169–11186.
- (57) Kresse, G.; Furthmüller, J. Efficiency of *Ab-Initio* Total Energy Calculations for Metals and Semiconductors Using a Plane-Wave Basis Set. *Comput. Mater. Sci.* **1996**, *6* (1), 15–50.
- (58) Blöchl, P. E. Projector Augmented-Wave Method. *Phys. Rev. B* **1994**, *50* (24), 17953–17979.
- (59) Kresse, G.; Joubert, D. From Ultrasoft Pseudopotentials to the Projector Augmented-Wave Method. *Phys. Rev. B* **1999**, *59* (3), 1758–1775.
- (60) Perdew, J. P.; Burke, K.; Ernzerhof, M. Generalized Gradient Approximation Made Simple. *Phys. Rev. Lett.* **1996**, *77* (18), 3865–3868.
- (61) Grimme, S.; Antony, J.; Ehrlich, S.; Krieg, H. A Consistent and Accurate *Ab Initio* Parametrization of Density Functional Dispersion Correction (DFT-D) for the 94 Elements H–Pu. *J. Chem. Phys.* **2010**, *132* (15), No. 154104.
- (62) Biesinger, M. C. Advanced Analysis of Copper X-ray Photoelectron Spectra. *Surface Interface Anal.* **2017**, *49* (13), 1325–1334.
- (63) Mishra, M. K.; Ramamurty, U.; Desiraju, G. R. Solid Solution Hardening of Molecular Crystals: Tautomeric Polymorphs of Omeprazole. *J. Am. Chem. Soc.* **2015**, *137* (5), 1794–1797.
- (64) Mishra, M. K.; Mishra, K.; Narayan, A.; Reddy, C. M.; Vangala, V. R. Structural Basis for Mechanical Anisotropy in Polymorphs of a Caffeine–Glutaric Acid Cocrystal. *Cryst. Growth Des.* **2020**, *20* (10), 6306–6315.
- (65) Duan, X.; Yuan, H.; Tang, W.; He, J.; Guan, X. A Phenomenological Primary–Secondary–Tertiary Creep Model for Polymer-Bonded Composite Materials. *Polymers* **2021**, *13* (14), 2353.
- (66) Wu, D.; Huang, X.; Duan, X.; Jiang, Y.; Shi, D.; Chang, L.; Zhang, L.; He, J. Static and Time-Dependent Plasticity of Monolithic Metal–Organic Frameworks. *J. Phys. Chem. C* **2023**, *127* (9), 4749–4758.
- (67) Lin, C.-Y.; Chen, Y.-C.; Lin, C.-H.; Chang, K.-V. Constitutive Equations for Analyzing Stress Relaxation and Creep of Viscoelastic Materials Based on Standard Linear Solid Model Derived with Finite Loading Rate. *Polymers* **2022**, *14* (10), 2124.
- (68) Sahu, R.; Patra, K.; Szpunar, J. Experimental Study and Numerical Modelling of Creep and Stress Relaxation of Dielectric Elastomers. *Strain* **2015**, *51* (1), 43–54.
- (69) Yamaguchi, K.; Thomas, A. G.; Busfield, J. J. C. Stress Relaxation, Creep and Set Recovery of Elastomers. *Int. J. Nonlinear Mech.* **2015**, *68*, 66–70.
- (70) Yu, K.; Jiang, Y.; Wright, C.; Hartland, G. V. Energy Dissipation for Nanometer Sized Acoustic Oscillators. *J. Phys. Chem. C* **2022**, *126* (8), 3811–3819.
- (71) Das, S.; Mondal, A.; Reddy, C. M. Harnessing Molecular Rotations in Plastic Crystals: A Holistic View for Crystal Engineering of Adaptive Soft Materials. *Chem. Soc. Rev.* **2020**, *49* (24), 8878–8896.
- (72) Wang, W.; Zhao, D.; Yang, J.; Nishi, T.; Ito, K.; Zhao, X.; Zhang, L. Novel Slide-Ring Material/Natural Rubber Composites with High Damping Property. *Sci. Rep.* **2016**, *6* (1), No. 22810.
- (73) Pelton, M.; Sader, J. E.; Burgin, J.; Liu, M.; Guyot-Sionnest, P.; Gosztoła, D. Damping of Acoustic Vibrations in Gold Nanoparticles. *Nat. Nanotechnol.* **2009**, *4* (8), 492–495.

(74) Bhogra, M.; Goodwin, A. L.; Cheetham, A. K.; Waghmare, U. V. Quantifying the Intrinsic Mechanical Flexibility of Crystalline Materials. *Phys. Rev. B* **2023**, *108* (21), No. 214106.